PHILOSOPHICAL TRANSACTIONS OF THE ROYAL SOCIETY A MATHEMATICAL, PHYSICAL & ENGINEERING SCIENCES

Rydberg electron wavepacket dymanics in atoms and molecules

J. A. Ramswell, V. G. Stavros, Q. Hong and H. H. Fielding

Phil. Trans. R. Soc. Lond. A 1998 **356**, 363-376
doi: 10.1098/rsta.1998.0170

The Royal Society

Rydberg electron wavepacket dynamics in atoms and molecules

By J. A. Ramswell, V. G. Stavros, Q. Hong and H. H. Fielding

Department of Chemistry, King's College London, Strand, London WC2R 2LS, UK

The generation and detection of Rydberg electron wavepackets using picosecond lasers is discussed with reference to the observation of the dynamics of spin-orbit autoionization in Xe. A multiphoton (nanosecond + picosecond) excitation scheme is employed with two-photon phase-sensitive detection, based on the observation of Ramsey interference fringes. To complement the experiment, time-dependent multichannel quantum-defect theory (TD-MQDT) calculations have been developed to investigate the dynamics of a spin-orbit autoionizing Rydberg wavepacket in Ar. The time-dependent partial photoionization cross-sections reveal interesting interference patterns in the recurrence spectra which are accounted for in terms of the quantum defects of the autoionizing channels. Finally, the rovibrational and rotational autoionization dynamics of a Rydberg wavepacket in H_2 are investigated using TD-MQDT. It is demonstrated that, in the time-domain, the configuration interaction between rotational channels can be described quantitatively in terms of an interaction time. In contrast to the rovibrational autoionization lifetime, which is determined by the classical orbit period ($\propto n^3$), the rotational autoionization lifetime is determined by the kinetic energy of the electron wavepacket following collision with the ion core.

Keywords: Rydberg electron dynamics; Rydberg wavepackets; spin-orbit autoionization dynamics; rovibrational autoionization; rotational autoionization; ultrafast laser

1. Introduction

Recent improvements in ultrafast lasers and detection methods have made it possible to investigate the classical aspects of the behaviour of Rydberg states using wavepackets. An electronic wavepacket is created by coherent superposition of several non-degenerate Rydberg eigenstates and is, therefore, a non-stationary state. Excitation from the ground state, or a low-lying electronically excited state, creates an electronic wavepacket which is localized within a few Bohr radii of the ion core (the transition dipole moment from a more tightly bound state is negligible at larger radial distances). The subsequent evolution of the wavepacket along a particular coordinate mimics a classical trajectory in the corresponding classical potential and has a characteristic period which corresponds to the classical oscillation time of a particle in the same potential well. For example, a superposition of several states with the same angular momentum l, but with different principal quantum number n, creates a bound Rydberg electron wavepacket which evolves in the radial coordinate (Wals *et al.* 1994). Initially, the wavepacket behaves classically, i.e. it passes through the core region at multiples of the classical orbit period $\tau_{\mathrm{cl}} = 2\pi\bar{n}^3$ (a.u.),

although at longer times the wavepacket may disperse. Following dispersion, the various components of the wavepacket will eventually rephase and the original classical picture become apparent; this is termed a full revival and occurs at $T_{\mathrm{R}} = \frac{1}{3}\bar{n}\tau_{\mathrm{cl}}$ (a.u.) (Wals *et al.* 1994). Partial revivals may be observed at fractions of the revival period, e.g. a second-order partial revival, in which the wavepacket is split into two smaller wavepackets which are π out of phase with one another, may be observed at time $\frac{1}{2}T_{\mathrm{R}}$. The precise time at which a partial or full revival occurs is determined by the phase shift introduced by the finite size of the ion core, $\delta = 2\pi\mu$, where μ is the quantum defect (in modulo one) (Wals *et al.* 1995*a*) commonly determined from conventional frequency-resolved spectroscopy. It is also possible to use wavepackets to investigate the interaction between different electronic configurations, i.e. to observe a time-resolved configuration interaction. In an interesting experiment, Schumacher *et al.* (1996) created a radial wavepacket in atomic Ba in the presence of a degenerate doubly excited Rydberg state and observed a temporal oscillation between configurations. Other recent Rydberg electron wavepacket experiments have involved exciting superpositions of several angular momentum states to create electron wavepackets that evolve in the angular coordinates. The dynamics of both bound and unbound angular electron wavepackets have been investigated in the presence of electric fields (Broers *et al.* 1993, 1994; Lankhuijzen & Noordam 1995) and parallel electric and magnetic fields (Fielding *et al.* 1995; Wals *et al.* 1995*b*).

2. Detection of Rydberg electron wavepackets

The major premise of Rydberg electron wavepacket production and detection is that the wavepacket is required to be at or near the ionic core for processes such as photoexcitation or photoionization to occur; this limitation greatly simplifies any detection technique employed to observe the temporal evolution of a wavepacket. Early experiments relied on a pump-probe technique to photoionize the Rydberg wavepacket (Yeazell & Stroud 1988; ten Wolde *et al.* 1988). In these experiments, a wavepacket was created by a picosecond pump pulse and allowed to evolve along its classical trajectory until a delayed picosecond probe pulse was applied to ionize the wavepacket. If the timing of the probe pulse coincided with the return of the wavepacket to the core, ionization was observed, whereas, if the wavepacket was at the outer turning point of its trajectory, relatively little ionization was observed. Unfortunately, further progress with this detection technique was hampered by the rather low signal intensities obtained due to the relatively small probability of photoionizing high Rydberg states (approximately 10^{-4}). To overcome this problem a more efficient experimental approach, based on the observation of Ramsey interference fringes, was proposed by Noordam *et al.* (1992) and subsequently exploited widely (see, for example, Broers *et al.* 1993; Christian *et al.* 1993; Jones *et al.* 1993; Wals *et al.* 1994; Fielding *et al.* 1995; Noel & Stroud 1995; Schumacher *et al.* 1996). In these experiments, the return of an electron wavepacket to its initial state, at time $t = 0$, after a time $t = \tau$ (i.e. its autocorrelation function $\langle\psi(\tau)|\psi(0)\rangle$) is monitored by creating two identical electron wavepackets in the atom with a well-defined delay and phase difference. The total Rydberg population depends on both the position of the first wavepacket at the time of creation of the second wavepacket and the precise phase relationship between the two. If, when the first wavepacket has returned to the core region, the second wavepacket is created in phase with the first, an enhancement of excited-state population is observed. Conversely, if it is created out of phase,

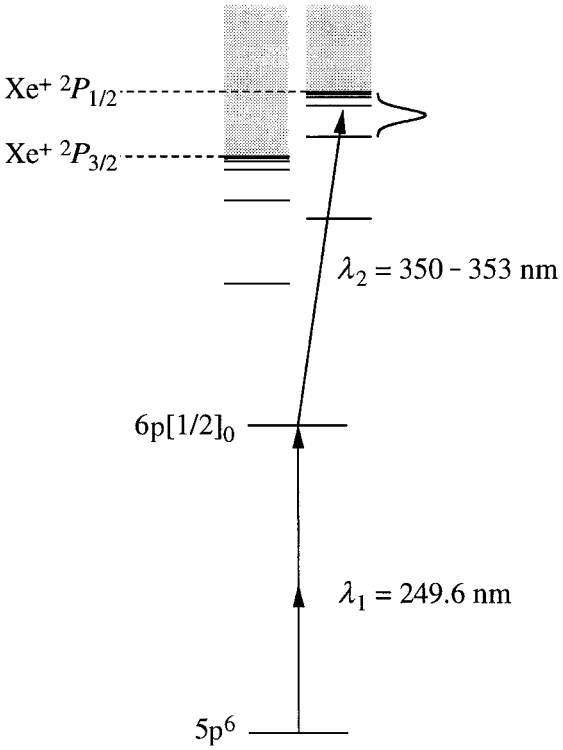

Figure 1. A schematic energy-level diagram illustrating the multiphoton excitation of a coherent superposition of autoionizing and continuum states between the $^2P_{3/2}$ and $^2P_{1/2}$ ionization limits (dashed lines) of Xe.

there is a depletion of excited-state population. On the other hand, if the second wavepacket is created whilst the first wavepacket is away from the core, there can be no interference and the signal is simply the sum of the excited state populations of the individual wavepackets. Good quality recurrence spectra may then be obtained by scanning several such Ramsey interference fringes and plotting the root mean square of the Rydberg population at a series of times, τ.

3. The dynamics of spin-orbit autoionization in Xe: experiment

All previous experiments to observe electron dynamics in atoms in the absence of external fields have concentrated on bound motion in the radial coordinate. In this paper we present an experiment to observe the dynamics of a quasibound radially localized Rydberg wavepacket created above the lowest spin-orbit ionization limit in Xe. Previous Rydberg wavepacket experiments have been performed in atoms with relatively low ionization potentials, such as Na, Rb and Ba; by contrast, the noble gases have relatively high ionization potentials and, therefore, it is impossible to access their high Rydberg states simply using the frequency upconverted output of a commercial picosecond laser. In the experiment described here, a coherent superposition of autoionizing Rydberg states of Xe, with average principle quantum number $n = 40$, is excited in a resonance-enhanced excitation process. The excitation scheme is illustrated in figure 1.

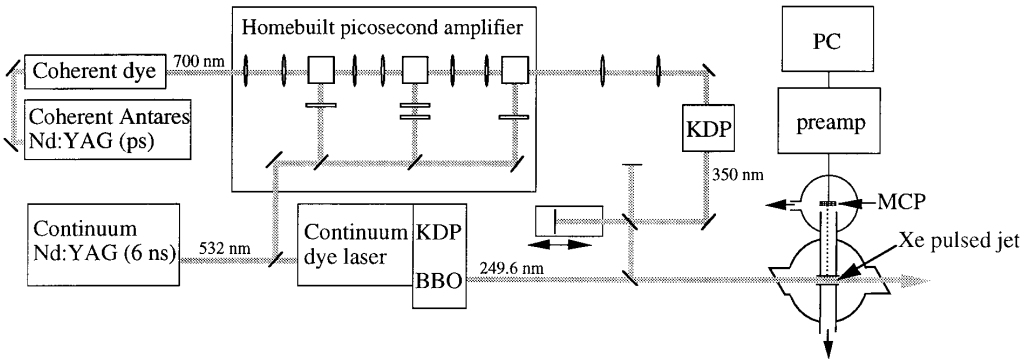

Figure 2. Schematic diagram of the experimental set up for a multiphoton phase-sensitive experiment to observe the dynamics of Rydberg electron wavepackets in atoms and molecules.

(*a*) *Experiment*

A schematic diagram of the experimental setup is presented in figure 2. 180 mJ of 532 nm radiation from a nanosecond Nd:YAG (Continuum Powerlite 8020) pumped dye laser (Continuum ND6000) is frequency doubled and then mixed with the fundamental 1064 nm radiation from the Nd:YAG to generate radiation at 249.6 nm (2–3 mJ, 6 ns, 20 Hz). This narrow bandwidth radiation is set to be in two-photon resonance with the $6p[0\frac{1}{2}]_0 \leftarrow 5p$ transition in Xe at 80 119.474 cm^{-1} (Moore 1958). 1.5 W of 532 nm radiation from a picosecond modelocked Nd:YAG laser (Coherent Antares) is used to synchronously pump an ultrafast dye laser (Coherent 701 series) to produce a 76 MHz train of pulses with autocorrelation width 2.2 ps and average power 200 mW. These pulses are amplified at 20 Hz, using 120 mJ of light from the nanosecond Nd:YAG laser to pump a series of Bethune cells (1 mm; 4 mm; 8 mm), and then frequency doubled in KDP to generate picosecond radiation at around 350 nm with a bandwidth of greater than 7 cm^{-1}. These pulses are subsequently split into two equal pulses at a thin (2 mm) beamsplitter and enter a stabilized Michelson interferometer arrangement to introduce a delay with precisely determined phase difference with fluctuations of less than $\pm\frac{1}{5}\pi$ (corresponding to less than $\pm$15 nm). One of the arms of the interferometer consists of a mirror mounted on top of a piezo positioner (Physik Instrumente P-780) which is in turn mounted on a DC motor-controlled translation stage (Physik Instrumente M-510). The piezo positioner is capable of moving in stepsizes of less than 10 nm and is used to provide the well-defined phase difference between the two optical pulses. The DC motor-controlled translation stage moves in stepsizes of around 20 μm and is used to change the coarse delay between the two optical pulses, and hence to track the wavepacket along its trajectory.

To stabilize the interferometer a low repetition-rate feedback system has been developed (figure 3) which is a modification of one described for a high repetition-rate experiment by Scherer *et al.* (1991). The stabilization system itself consists of three units: a CCD array, a comparison circuit, and a PID feedback circuit. The CCD array monitors variations in the precise delay between a pair of reference beams created in the interferometer. The reference beams are provided by the output of a stable continuous He–Ne laser (Carl Zeiss Jena, LGK7628; 15 mW at 632.814 nm) which enters the interferometer almost collinearly with the picosecond light. When the piezo and motor translation stages are first moved to a new delay position, the intensities of the reference fringes at each pixel of the CCD array are read and the mean intensity

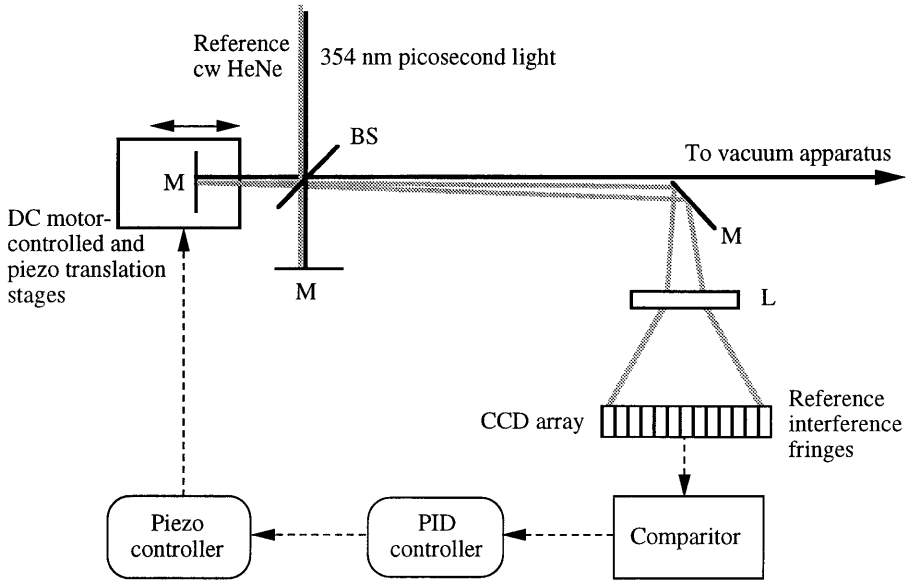

Figure 3. Schematic diagram illustrating the interferometer and stabilization circuit. Note that two mirrors are mounted on the piezo and DC motor-controlled translation stages, one to ensure that the two picosecond pulses leave the interferometer collinearly whilst the other is mounted at a small angle so that the two HeNe reference beams diverge upon leaving the interferometer.

is deduced (by averaging the maximum and minimum) and stored digitally, together with the number of the first CCD pixel at which the measured intensity corresponds to the mean. Subsequently, the intensity read at this selected pixel is compared continuously with the stored value until a new scan command is received by the comparison circuit, during which time it is temporarily non-functional. Should the instantaneous intensity at this pixel differ from the mean, an error signal is generated which is proportional to the intensity difference and passed on to the PID circuit. Scanning the phase difference between the two optical pulses is realized by the same circuit. Each time a scan command is received by the comparison circuit, the pixel number stored by the comparison circuit is first modified to be the old value plus the number of pixels equivalent to the preprogrammed stepsize. The stabilization circuit then forces the piezo to a new position via the PID circuit where the new reference fringe pattern satisfies the intensity value at the new pixel number. Using this scheme, the scan step size cannot be larger than a quarter of a wavelength of the reference beam; however, this is not a problem in our experiments since larger steps may be realized by moving the dc motor-controlled translation stage or by making a series of smaller piezo movements.

After the interferometer, the pair of delayed picosecond UV pulses are focused collinearly with the nanosecond radiation into a pulsed jet of Xe to excite a superposition of Rydberg states converging to the upper spin-orbit ionization limit, $^2P_{1/2}$. Following excitation, a 2 kV cm^{-1} pulsed electric field applied across the excitation region accelerates Xe^+ ions along a 20 cm flight tube towards a multichannel plate detector with approximately 100% efficiency. The measured ion current is proportional to the total Rydberg electron population following excitation by the pair of delayed picosecond laser pulses. In a typical phase-sensitive measurement, autoionizing ion current is averaged over approximately 40 laser shots at a given delay.

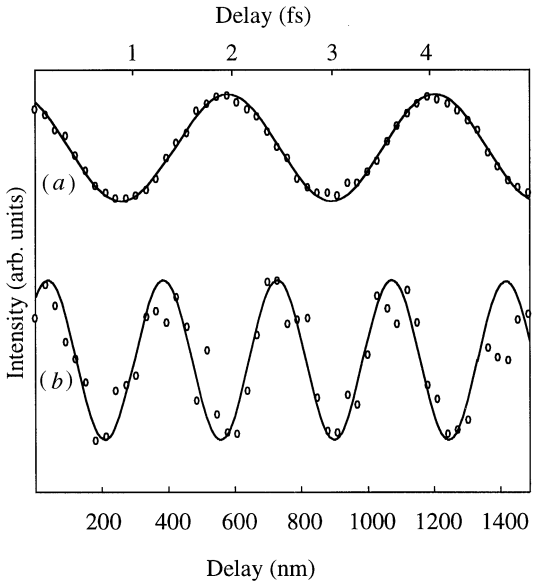

Figure 4. Experimentally measured interference fringes (open circles) obtained using the stabilization circuit created: (*a*) by focusing a single HeNe reference fringe on a photodiode; and (*b*) by monitoring ion current following excitation of two autoionizing Rydberg wavepackets in Xe.

(*b*) *Results*

Examples of Ramsey interference fringes obtained using our experimental scheme are presented in figure 4. Figure 4*a* represents a measurement of the intensity of a single HeNe fringe focused onto a photodiode as a function of delay (in both nanometres and femtoseconds), introduced by scanning the piezo in the variable arm of the interferometer. Each open circle is an experimentally recorded intensity obtained after averaging over 1 s whilst the solid curve is a fit. Note that a near-perfect sinusoidal trace is obtained with a period equivalent to the wavelength of the HeNe radiation (632.8 nm), illustrating the stability of the interferometer. Figure 4*b* is a measure of total ion current at around $t = 0$ following excitation of two identical autoionizing electron wavepackets in Xe. Ramsey interference fringes are observed with a period corresponding to excitation with light at 354 nm. The open circles are experimetally measured data points after averaging over 40 laser shots (2 s) whereas the solid sinusoidal curve is a fit. It should be noted that the noise in the Ramsey fringes is a result of fluctuations in the intensity of the amplified picosecond laser pulses.

An example of a recurrence spectrum of an autoionizing Rydberg wavepacket in Xe is presented in figure 5. The solid line represents experimental data obtained by averaging over 20 laser shots per piezo step and approximately eight piezo steps per Ramsey fringe. Sets of five Ramsey fringes are recorded for each coarse delay step. The fringes are fitted with a sinusoidal wave of the correct frequency, the RMS of the fitted wave is deduced and a moving average of eight RMS values calculated. The dotted line is calculated from the autocorrelation function of the wavepacket $\langle \Psi(0) | \Psi(t) \rangle$, where

$$\Psi(t) = \sum_{ns,nd} a_{nl} g_{nl} R_{nl}(r) \mathrm{e}^{-\mathrm{i}\omega_{nl} t} \mathrm{e}^{\Gamma_{nl} t}. \tag{3.1}$$

a_{nl} are the dipole transition moments from the ground state and g_{nl} are amplitude

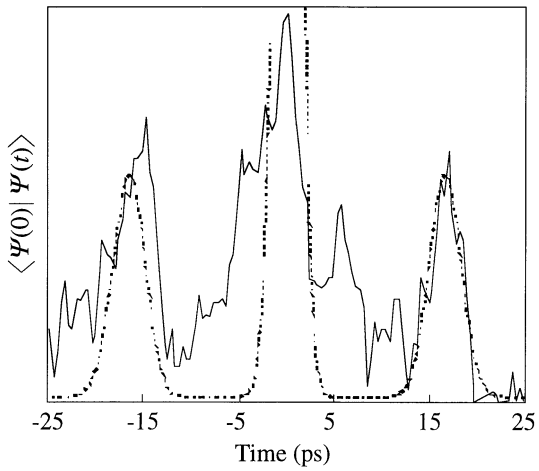

Figure 5. Experimentally measured recurrence spectrum (solid line) of an autoionizing Xe Rydberg wavepacket with $\bar{n} = 47.5$ (orbit period 16.3 ps). The dotted line represents the autocorrelation function of the wavepacket $\langle \Psi(0)|\Psi(t)\rangle$ calculated using parameters decribed in the text.

factors determined by the excitation profile, which is assumed to be Gaussian with a FWHM of 7 cm^{-1}. $R_{nl}(r)$ are the radial wavefunctions (Ya Baranov 1997, personal communication), $\mathrm{e}^{-\mathrm{i}\omega_{nl}t}$ the usual phase factors and Γ_{nl} the autoionization rates (Wang & Knight 1986). The orbit period is around 16.3 ps, corresponding to excitation around average principal quantum number $\bar{n} = 47.5$. To the best of our knowledge, this is the first observation of a spin-orbit autoionizing Rydberg electron wavepacket.

4. The dynamics of spin-orbit autoionization in Ar: a time-dependent multichannel quantum defect theory approach

To complement the experiment described in § 3, we have developed a time-dependent multichannel quantum-defect theory (TD-MQDT) to investigate the dynamics of spin-orbit autoionizing atomic Rydberg wavepackets. In the calculations presented here, an autoionizing Rydberg wavepacket is created in Ar by coherent excitation of several 'bound' $ns'[\frac{1}{2}]_1$ and $nd'[\frac{3}{2}]_1$ levels converging to the upper $j^+ = \frac{1}{2}$ spin-orbit state of the ion. Classically, the wavepacket orbits in the radial coordinate with period $\tau_{\mathrm{cl}} = 2\pi\bar{n}^3$, where $\bar{n}$ is a measure of the average energy below the ionization limit, $\bar{n} = (-2\varepsilon_{1/2})^{-1/2}$. Each time the wavepacket passes through the core region, some of the Rydberg population scatters into the $\mathrm{s}[\frac{3}{2}]_1$, $\mathrm{d}[\frac{1}{2}]_1$ and $\mathrm{d}[\frac{3}{2}]_1$ continua associated with the $j^+ = \frac{3}{2}$ state of the ion. Continuum states excited at $t = 0$ never return to the core but escape to infinity immediately.

Time-dependent photoionization cross-sections to each of the three open channels are calculated using:

$$\sigma_i(t) \propto \left| \int \mathrm{d}E \exp\left[-2\ln 2 \frac{(E - E_0)^2}{\Delta E^2} \right] E^{1/2} d_i^{(-)}(E, t) \right|^2 . \tag{4.1}$$

$\Delta E = 0.441/\tau_{\mathrm{L}}$ (a.u.) is the FWHM of a bandwidth-limited optical pulse with a Gaussian profile and width τ_{L}. E_0 is the average energy of the laser pulse. The partial photoionization cross-sections are calculated using MQDT (Ramswell & Fielding

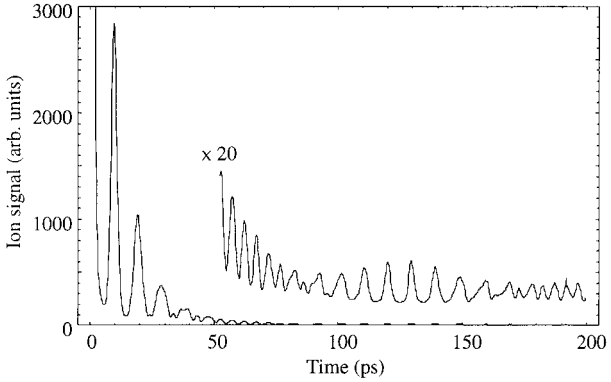

Figure 6. Time-resolved photoionization cross-section following excitation of an autoionizing wavepacket in Ar with $\bar{n} = 40$ using a bandwidth-limited Gaussian laser pulse of length $\tau_{\mathrm{L}} = 2$ ps.

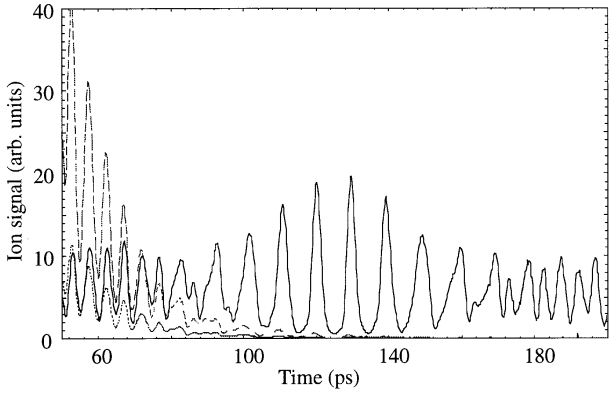

Figure 7. Time-resolved partial photoionization cross-sections to the $\mathrm{s}[\frac{3}{2}]_1$ (bold line), $\mathrm{d}[\frac{1}{2}]_1$ (dashed line) and $\mathrm{d}[\frac{3}{2}]_1$ (dotted line) channels following excitation around $\bar{n} = 40$ in Ar.

1998) and the total time-dependent photoionization cross-section is simply an incoherent sum of the partial cross-sections:

$$\sigma(t) = \sum_{i \in o} \sigma_i(t). \tag{4.2}$$

The total time-dependent photoionization cross-section following excitation around $\bar{n} = 40$ with a laser pulse of width $\tau_{\mathrm{L}} = 2$ ps is presented in figure 6. Initially, peaks are observed in the recurrence spectrum at multiples of the orbit period, $\tau_{\mathrm{cl}} = 9.7$ ps. The overall decay of the total photoionization cross-section reflects the lifetime of the $n\mathrm{d}'[\frac{3}{2}]_1$ series since most of the oscillator strength lies in the transitions to these short-lived $n\mathrm{d}'$ states. Both the second partial revival at around 64.9 ps and the first full revival around 129.7 ps are observed clearly in the magnified portion of the recurrence spectrum.

Partial photoionization cross-sections to each of the open channels are presented in figure 7 ($\mathrm{s}[\frac{3}{2}]_1$ bold line; $\mathrm{d}[\frac{1}{2}]_1$ dashed line; $\mathrm{d}[\frac{3}{2}]_1$ dotted line). The orbital angular momentum of the electron does not change during the autoionization process; i.e. the $n\mathrm{s}'$ series is coupled to the s continuum whereas the $n\mathrm{d}'$ series is coupled to the d continuum. Whilst most of the initial photoionization cross-section may be attributed to the rapidly autoionizing $n\mathrm{d}'$ series, at longer times only the $n\mathrm{s}'$ contribution to

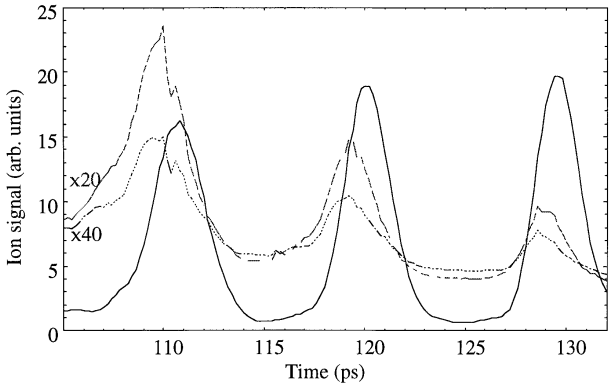

Figure 8. A comparison between the interference patterns in the photoionization cross-sections of the different angular momentum components of an Ar wavepacket. The curves represent partial photoionization cross-sections to the $s[\frac{3}{2}]_1$ (bold line), $d[\frac{1}{2}]_1$ (dashed line) and $d[\frac{3}{2}]_1$ (dotted line) continua.

the wavepacket survives to contribute to the photoionization signal. Thus, the radially localized wavepacket may initially be considered as possessing predominantly $l = 2$ angular momentum character but gradually evolves into a wavepacket possessing predominantly $l = 0$ character. It will be interesting to determine the classical trajectory of such a radially localized wavepacket with mixed angular momentum character and to observe the evolution of the angular momentum from $l = 2$ to $l = 0$.

An expanded portion of the recurrence spectrum around the time of the first full revival is presented in figure 8 to emphasize the relative phase shift of the interference patterns in the photoionization cross-sections of the different angular momentum components of the wavepacket. Close to the position of the full revival, $T_{\mathrm{R}} = 129.7$ ps, autoionization into the s continuum lags autoionization into the d continua by approximately 0.64 ps, corresponding to $0.07\tau_{\mathrm{cl}}$. This phase shift corresponds to the difference between the quantum defects of the two autoionizing series in modulo one. ($\mu = 2.14$ and 0.21 for the $ns'[\frac{1}{2}]_1$ and $nd'[\frac{3}{2}]_1$ series, respectively (Koeckhoven *et al.* 1994) and the difference in modulo one is 0.07.) This phase shift can be explained by making a Taylor expansion of the phase factors of the stationary states of which the wavepacket is composed (Wals *et al.* 1995*a*).

5. The dynamics of rotational and rovibrational autoionization in H_2: a time-dependent multichannel quantum defect theory approach

Surprisingly, although a great deal of interest has been directed towards the investigation of electron wavepacket dynamics in atoms, there has been little interest in electron wavepacket dynamics in molecular systems where there is the possibility of rotation and vibration of the molecular ion core. Hughes & Meacher (1994) have calculated how the vibration frequency of a molecule varies with the evolution of an electron wavepacket created in the molecule whilst Fielding (1994) has demonstrated the effect of a rotating core on the dynamics of an electron wavepacket. The calculations presented here demonstrate the advantage of employing an electron wavepacket approach to molecular Rydberg dynamics to explain rovibrational and rotational autoionization from a semiclassical viewpoint.

The situation being modelled is illustrated in figure 9. A coherent superposition

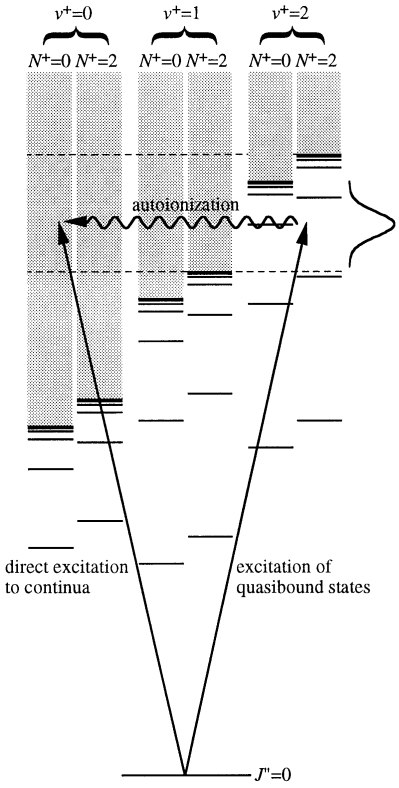

Figure 9. A schematic energy level diagram illustrating the excitation of a coherent superposition of autoionizing and continuum states, between the $v^+ = 1$ and $v^+ = 2$ ionization limits (dashed lines), in para-H_2.

of autoionizing and continuum states is excited in the energy region between the $v^+ = 1$ and $v^+ = 2$ ionization limits of para-H_2, as indicated by the dashed lines. The superposition of continuum states creates a wavepacket that escapes to infinity immediately, whereas, the superposition of autoionizing states creates a wavepacket that, at the time of its creation, is localized in the core region. The quasibound electronic wavepacket travels to large distances from the ion core and is then reflected back by the Coulomb potential, returning at times $\tau_i = 2\pi\bar{n}_i^3$, where $\bar{n}_i = (-2\varepsilon_i)^{-1/2}$ is a measure of the average excitation energy below a particular rovibrational ionization limit i. Upon its return, the wavepacket scatters from the molecular ion core and some of the electronic wavepacket may leak into the continua and escape to infinity. The process repeats itself until autoionization is complete.

Time-dependent partial photoionization cross-sections to each open channel, $\sigma_i(t)$, are calculated by integrating the partial dipole transition moments, $d_i^{(-)}(E,t)$, over the bandwidth of the excitation pulse using equation (4.1). The dipole transition moments $d_i^{(-)}(E,t)$ are calculated using the usual methods of MQDT (Greene & Jungen 1985) adapted for TD-MQDT (Fielding 1994, 1997).

(*a*) *Rovibrational autoionization*

Below both the $v^+ = 2$, $N^+ = 0$ and $v^+ = 2$, $N^+ = 2$ ionization limits, two interleaved Rydberg series, $nP0$ and $nP2$, are observed in the photoabsorption spectrum. The autoionizing resonances appear superimposed on a flat background with

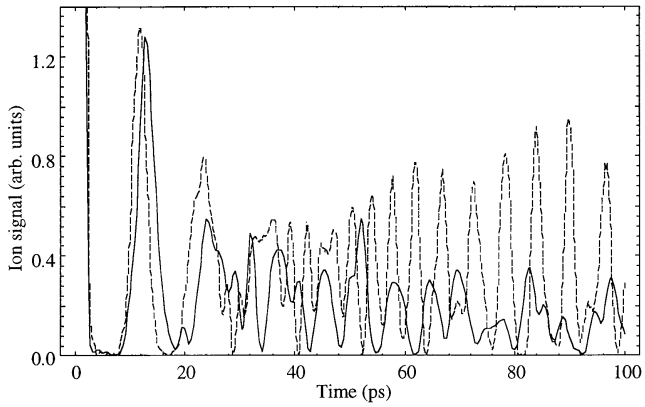

Figure 10. A comparison between time-resolved partial cross-sections to the $v^+ = 1$, $N^+ = 0$ channel both with (solid line) and without (dashed line) configuration interaction, following excitation around $\bar{n}_0 = 42.5$ with a 1.7 ps pulse. Note that the effect of the configuration interaction is to shift the first peaks to longer times by approximately 1.4 ps.

characteristic asymmetric Fano profiles (Fano 1961) and, in the frequency domain, configuration interaction between the two Rydberg series manifests itself as perturbations to transition energies, intensities and lineshapes.

How does the configuration interaction influence the dynamics of rovibrational autoionization? The answer to this question is apparent in figure 10 which presents a direct comparison between the time-resolved partial cross-sections to the $v^+ = 1$, $N^+ = 0$ channel both with (solid line) and without (dashed line) configuration interaction, following excitation around $\bar{n}_0 = 42.5$ with a 1.7 ps pulse. The calculation neglecting configuration interaction is an artificial scenario in which the $N^+ = 2$ channel is omitted, i.e. a three-channel calculation including $v^+ = 0$, 1 and 2 with $N^+ = 0$ only. Peaks are observed in both recurrence spectra, to a first approximation, at multiples of the orbit period of an electronic wavepacket with average principle quantum number $\bar{n}_0$, indicating that each time the wavepacket returns near the core it has a chance of being scattered into the ionization continua. There is, however, an obvious difference between the two spectra. Namely that the first two peaks in the full six-channel calculation are shifted to longer times than those in the three-channel calculation, by approximately 1.4 ps. At later times, once the wavepacket has dispersed to such an extent that it is more or less completely delocalized, the interference patterns observed in the three- and six-channel calculations become dissimilar. It is worth noting that, in the three-channel calculation, the wavepacket generated by coherent superposition of several unperturbed Rydberg states undergoes similar dynamics to those observed in hydrogenic atoms (Wals *et al.* 1994, 1995*a*). Second-, third- and fourth-order partial revivals are observed quite clearly at approximately 83 ps, 55 ps and 41 ps, respectively. It is also worth commenting that the autoionization lifetime is longer for a wavepacket created in the absence of the $N^+ = 2$ channel. States converging to the higher $N^+ = 2$ ionization limit, in the same region of the spectrum, are of lower principle quantum number and, therefore, have shorter autoionization lifetimes.

The observed phase shift of the peaks in the recurrence spectrum calculated including configuration interaction (*ca.* 10% of the orbit period) can be attributed to $N^+ = 0/N^+ = 2$ channel interactions. To justify this quantitatively, a comparison between the classical orbit period for excitation around $\bar{n}_0 = 50.8$ ($\bar{n}_2 = 23.5$) in

Table 1. *A comparison between the measured orbit periods, τ_{MQDT}, for excitation around $\bar{n}_0 = 50.8$ ($\bar{n}_2 = 23.5$) with various bandwidth-limited Gaussian laser pulses of length τ_{L} and bandwidths ΔE*
($\Delta\tau = \tau_{\mathrm{MQDT}} - \tau_{\mathrm{cl}}$ is the phase shift introduced by the configuration interaction, in ps, and $\Delta\tau/\tau_{\mathrm{cl}}$ is the phase shift as a fraction of the classical orbit period τ_{cl}.)

τ_{L} (ps)	ΔE (cm^{-1})	τ_{MQDT} (ps)	$\Delta\tau$ (ps)	$\Delta\tau/\tau_{\mathrm{cl}}$
1.7	8.7	22.1	2.2	0.11
4.0	3.7	21.2	1.3	0.07
10.0	1.5	20.9	1.0	0.05

the absence of interchannel interactions, and the time taken for the first peak in the photoionization spectrum to appear following coherent excitation of the perturbed $nP0$ series, as a function of laser bandwidth, is presented in table 1. Decreasing the bandwidth (increasing the pulse length) reduces the number of states most strongly perturbed by the nearby $23P2$ and $24P2$ levels included in the superposition and causes a corresponding decrease in the observed phase shift, i.e. reducing the configuration interaction reduces the phase shift.

Thus, observing the autoionization of an electronic wavepacket in H_2 in real time, allows one to measure an *interaction time* between rotational channels.

(*b*) *Rotational autoionization*

The total photoionization cross-section for excitation of $J' = 1$ levels from the $J'' = 0$ level in para-H_2 between the $v^+ = 2$, $N^+ = 0$ and $v^+ = 2$, $N^+ = 2$ ionization limits show a regular series of transitions to the $nP2$ levels which appear as dips in the photoionization cross-section, i.e. $q = 0$ (Fano 1961). Time-resolved partial photoionization cross-sections to the $v^+ = 1$ (top), and 2 (bottom) vibrational channels with $N^+ = 0$ (dashed) and 2 (solid), corresponding to excitations around $\bar{n}_2 = 33.0$, 49.3 and 60.0 with a bandwidth-limited Gaussian laser pulse with $\tau_{\mathrm{L}} = 1.2$ ps and bandwidth $\Delta E = 12.3\,\mathrm{cm}^{-1}$ are presented in figure 11. Peaks are observed in the $v^+ = 1$ cross-sections (rovibrational autoionization) at multiples of the classical orbit period of the electron wavepacket, i.e. whenever the electron wavepacket collides with the ion core it may gain sufficient energy to ionize at the expense of the rovibrational energy of the molecular ion. On the other hand, the partial cross-sections to the $v^+ = 2$, $N^+ = 0$ channel have a distinctly different appearance. First of all, it should be noted that pure rotational autoionization is the preferred autoionization pathway by more than a factor of 20, although very few electrons are observed in the $v^+ = 2$, $N^+ = 0$ continuum at $t = 0$. In addition, the rotational autoionization lifetime is observed to decrease with increasing $\bar{n}_2$, in contrast to rovibrational autoionization. This observation can be explained using the following picture: upon creation, the wavepacket undergoes an immediate collision with the core and, before the wavepacket has a chance to leave the core region, the rotational and electronic energies are exchanged leaving the electron wavepacket in a positive energy state and the molecular ion core in a rotationless state ($N^+ = 0$).

The plots presented in figure 12 enable one to compare directly both the classical orbit period as a function of $\bar{n}_2$ and the time taken for the first peak to appear in the purely rotational autoionization recurrence spectrum for each vibrational state of the ion core $v^+ = 0$, 1 and 2. Thus, although the classical orbit period ($\propto n^3$) determines

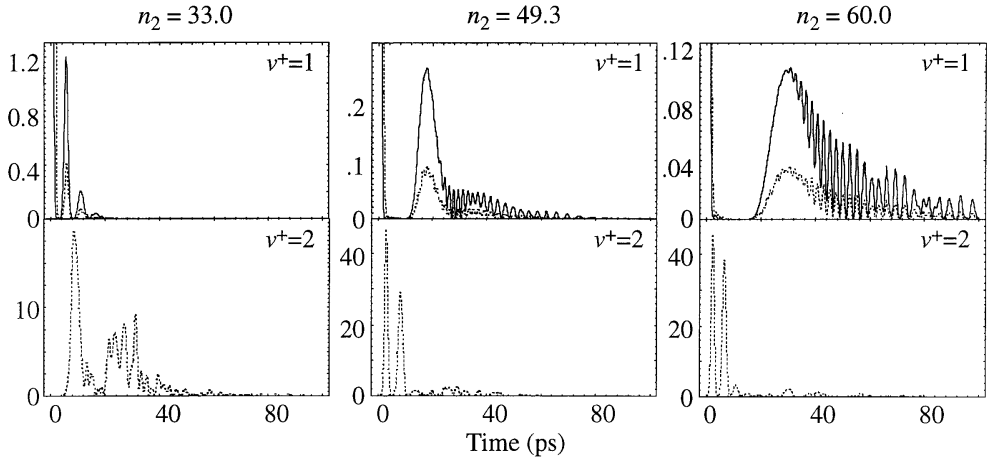

Figure 11. Time-resolved partial photoionization cross-sections to the $v^+ = 1$ (top row) and $v^+ = 2$ (bottom row) vibrational channels with $N^+ = 0$ (dashed lines) and $N^+ = 2$ (solid lines) corresponding to excitations around $\bar{n} = 33.0$, 49.3 and 60.0.

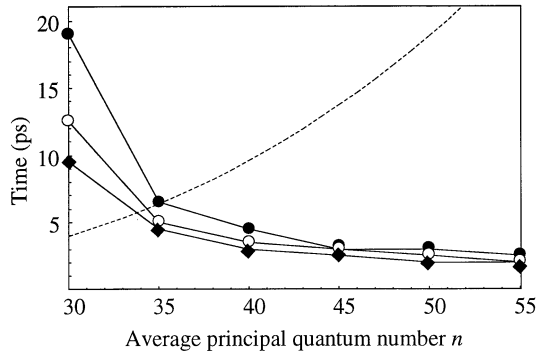

Figure 12. The variation of rotational autoionization time with average principal quantum number n for the $v^+ = 0$ (diamonds), $v^+ = 1$ (open circles) and $v^+ = 2$ (filled circles) vibrational states of the ion core. The dashed line corresponds to the classical orbit period $\tau_{cl} = 2\pi n^3$.

the rovibrational autoionization lifetime, it appears that it is the kinetic energy of the electron wavepacket, following collision with the ion core, that determines the rotational autoionization lifetime.

6. Conclusion

The generation and detection of an autoionizing Rydberg wavepacket in Xe has been presented together with complementary TD-MQDT calculations of the dynamics of spin-orbit autoionization in Ar. By observing time-dependent partial photoionization cross-sections, it becomes apparent that the angular momentum character of the wavepacket varies with time. In addition, the difference between the quantum defects of the s′ and d′ angular momentum components of the wavepacket gives rise to a shift in the interference patterns of the cross-sections to the s and d continua, equivalent to the quantum defect difference in modulo one times the classical orbit period. The envelopes of the recurrence spectra remain unchanged.

In a separate application of TD-MQDT to the rovibrational and rotational autoion-

ization dynamics of a Rydberg wavepacket in H_2, the configuration interaction between rotational channels is shown to manifest itself as a phase shift of the recurrence spectrum and provide a quantitative measure of the strength of the interaction in terms of an interaction time. Whereas the rovibrational autoionization lifetime is determined by the electronic orbit period and is proportional to n^3, the rotational autoionization lifetime is governed by the kinetic energy of the electron wavepacket following collision with the ion core.

We are grateful to the EPSRC and Royal Society for funding for equipment, the Leverhulme Trust for a postdoctoral fellowship (Q.H.) and the EPSRC for studentships (J.A.R. and V.G.S.). We also acknowledge Mr A. Hotouras for performing the calculations for figure 12 and Dr C. J. Barnett, from Imperial College London, for his help in building the stabilized interferometer.

References

Broers, B., Christian, J. F., Hoogenraad, J. H., van der Zande, W. J., van Linden van den Heuvell, H. B. & Noordam, L. D. 1993 *Phys. Rev. Lett.* **71**, 344–347.

Broers, B., Christian, J. F. & van Linden van den Heuvell, H.B. 1994 *Phys. Rev.* A **49**, 2498–2507.

Christian, J. F., Broers, B., Hoogenraad, J. H., van der Zande, W. J. & Noordam, L. D. 1993 *Opt. Commun.* **103**, 79–84.

Fano, U. 1961 *Phys. Rev.* **124**, 1866–1878.

Fielding, H. H. 1994 *J. Phys.* B **27**, 5883–5891.

Fielding, H. H. 1997 *J. Chem. Phys.* **106**, 6588–6595.

Fielding, H. H., Wals, J., van der Zande, W. J. & van Linden van den Heuvell, H. B. 1995 *Phys. Rev.* A **51**, 611–619.

Greene, C. H. & Jungen, Ch. 1985 *Adv. At. Mol. Phys.* **21**, 51–121.

Hughes, I. G. & Meacher, D. R. 1994 *J. Phys. B: At. Mol. Opt. Phys.* **27**, 1377–1386.

Jones, R. R., Raman, C. S., Schumacher, D. W. & Buchsbaum, P. H. 1993 *Phys. Rev. Lett.* **71**, 2575–2578.

Koeckhoven, S. M., Buma, W. J. & de Lange, C. A. 1994 *Phys. Rev.* A **49**, 3322–3332.

Lankhuijzen, G. M. & Noordam, L. D. 1995 *Phys. Rev.* A **52**, 2016–2028.

Moore, C. E. 1958 Atomic energy levels III. US National Bureau of Standards, circ. 467.

Noel, M. W. & Stround Jr, C. R. 1995 *Phys. Rev. Lett.* **75**, 1252–1255.

Noordam, L. D., Duncan, D. I. & Gallagher, T. F. 1992 *Phys. Rev.* A **45**, 4734–4737.

Ramswell, J. A. & Fielding, H. H. 1998 *J. Chem. Phys.* (Submitted.)

Scherer, N. F., Carlson, R. J., Matro, A., Du M., Ruggiero, A. J., Romero-Rochin, V., Cina, J. A., Fleming, G. R. & Rice, S. A. 1991 *J. Chem. Phys.* **95**, 1487–1511.

Schumacher, D. W., Duncan, D. I., Jones, R. R. & Gallagher, T. F. 1996 *J. Phys. B: At. Mol. Opt. Phys.* **29**, L397–L403.

ten Wolde, A., Noordam, L. D., Lagendijk, A. & van Linden van den Heuvell, H. B. 1988 *Phys. Rev. Lett.* **61**, 2099–2101.

Wals, J., Fielding, H. H., Christian, J. F., Snoek, L. C., van der Zande, W. J. & van Linden van den Heuvell, H. B. 1994 *Phys. Rev. Lett.* **72**, 3783–3786.

Wals, J., Fielding, H. H. & van Linden van den Heuvell, H. B. 1995*a* *Physica Scripta* T **58**, 62–68.

Wals, J., Fielding, H. H. & van Linden van den Heuvell, H. B. 1995*b* *Mod. Phys. Lett.* B **9**, 1845–1871.

Wang Liang-guo & Knight, R. D. 1986 *Phys. Rev.* A **34**, 3902–3907.

Yeazell, J. A. & Stround Jr, C. R. 1988 *Phys. Rev. Lett.* **60**, 1494–1497.